Pronounced postseismic deformation following a moderate normal-faulting earthquake: insights from the 2020 Mw 5.6 Dingri earthquake, Tibet

Lidong Bie,[1] Conor Rutland[1]

[1]School of Environmental Sciences, University of East Anglia, NR4 7TJ. E-mail: l.bie@uea.ac.uk

Summary

Stress accumulated on faults is released through both seismic and aseismic processes. Distinguishing and quantifying these modes is essential for seismic hazard assessment, as they control shaking intensity, aftershock triggering, and the rate at which faults regain strength following rupture. In this study, we investigate a moderate-magnitude (Mw 5.6) normal-faulting earthquake that occurred in 2020 in the highly dilatational Dingri region of southern Tibet. Our aim is to provide geodetic observations and modelling constraints on the post- to co-seismic moment ratio (PCMR) for moderate-magnitude earthquakes, which are currently underrepresented in the global catalogue. Our results indicate that approximately five years of afterslip accounts for 56.6% of the coseismic moment, placing this event among the highest PCMR values reported for normal-faulting earthquakes of this size. The lithological setting near the Lhagoi Kangri gneiss dome, including a siliciclastic sedimentary cover of at least 3 km, combined with localised high strain rate in the southern Pumqu-Xainza rift, likely promotes shallow aseismic slip and helps explain the elevated PCMR. Our results also highlight the difficulty of identifying active normal faults where geomorphic expression is subtle or inconsistent with expected surface features. Together, these results underscore the value of

ORIGINAL UNEDITED MANUSCRIPT

Downloaded from academic.oup.com/gji/advance-article/doi/10.1093/gji/ggag516/9121041 by East Anglia University user on 24 November 2026

© The Author(s) 2026. Published by Oxford University Press on behalf of The Royal Astronomical Society. This is an Open Access article distributed under the terms of the Creative Commons Attribution License (https://creativecommons.org/licenses/by/4.0/), which permits unrestricted reuse, distribution, and reproduction in any medium, provided the original work is properly cited.

22 interseismic coupling analyses for mapping asperities and creeping sections, as well as for
23 assessing strain partitioning on conjugate normal faults.

24

25 Keywords: Satellite geodesy; Seismic cycle; Asia; Continental tectonics: extensional.

26

Downloaded from academic.oup.com/gji/advance-article/doi/10.1093/gji/ggag516/9121041 by East Anglia University user on 24 November 2026

ORIGINAL UNEDITED MANUSCRIPT

1. Introduction

Earthquakes release accumulated tectonic stress within seconds, but a significant portion of strain is also released through a process known as afterslip (e.g., Churchill et al., 2022; Hawthorne et al., 2016). Afterslip is defined as post-earthquake slow slip on nearby fault sections relieving static coseismic stress change (Burgmann 2008). Afterslip is largely aseismic and transient, often referred to as the main mechanism explaining the temporal and spatial evolution of near field deformation shortly after an earthquake (Wright et al., 2013).

While it is intuitive to expect that larger earthquakes, which generate greater stress changes, would produce proportionally larger afterslip, current observations challenge this assumption. For earthquakes with magnitudes (M) greater than 6, the post-/co-seismic moment ratio (PCMR) falls in an interquartile range of 9%-32% with a median value of 18% (Churchill et al., 2022). In contrast, smaller earthquakes (M < 5) can exhibit PCMR values exceeding 3 (Hawthorne et al., 2016). Alwahedi and Hawthorne (2019) examined PCMR for M4-5 earthquakes and reported a ratio of 0.45 – larger than those estimated for M > 6 earthquakes. Only a few PCMR estimates exist for earthquakes between M5-6. For example, by inverting geodetic observations, Fattahi et al (2015) reported a PCMR of 70% on the Ghazaband fault in Parkistan. These observations suggest that the contribution from afterslip to crustal deformation for small earthquakes may equal or even exceed that from coseismic rupture.

This counterintuitive trend suggests that physical properties governing PCMR are more complex than previously understood. For M>6 earthquakes, the magnitude independent PCMR is considered as an indicator of earthquake self-similarity

ORIGINAL UNEDITED MANUSCRIPT

Downloaded from academic.oup.com/gji/advance-article/doi/10.1093/gji/ggag516/9121041 by East Anglia University user on 24 November 2026

(Hawthorne et al., 2016). However, Chen and Lapusta (2009) suggests that, for small (M < 3) repeating earthquakes, the PCMR falls in a range of much higher values. The self-similar scaling therefore does not hold for the whole magnitude scales, and calls for a new look at the aseismic afterslip contribution to tectonic deformation in M<6 earthquakes.

This study adds observations for earthquakes between M5-6, which are even less reported for normal-faulting mechanism, compared to other mechanisms (e.g., Fattahi et al., 2015; Wimpenny et al., 2017). We analyse co- and post-seismic displacements associated with the 2020 Mw 5.6 Dingri earthquake. Our study reveals a significant ratio of postseismic to coseismic moment release for a moderate-magnitude normal-faulting earthquake. These analyses provide insights into faulting structures in a currently active extensional rifting regime, and more importantly, add cases to further understanding the partitioning of seismic and aseismic stress releases during the earthquake cycle.

2. Regional seismicity and tectonics

The Dingri region in southern Tibet has been highly seismically active in recent decades. A Mw 7.1 normal-faulting earthquake struck devastatingly in 2025, representing one of the largest instrumentally recorded normal-faulting events on the Tibetan Plateau. Prior to the 2025 earthquake, the area experienced two moderate normal-faulting events: one in 2015 (Mw 5.7) and another on 20th March, 2020 (Mw 5.6), which is the focus of this study. Geodetic observations provide excellent constraints on the fault geometry and slip distribution of these events, enabling investigation of faulting

ORIGINAL UNEDITED MANUSCRIPT

Downloaded from academic.oup.com/gji/advance-article/doi/10.1093/gji/ggag516/9121041 by East Anglia University user on 24 November 2026

processes, causative structures, and their interactions (e.g., He et al., 2026; Ma et al., 2026). Qiao et al. (2025) proposed that an incipient rift is developing here, featuring a young, immature graben bounded by the conjugate normal faults that ruptured in the 2025 earthquake sequence.

The collision of the Indian and Eurasian Plates built a high plateau characterised by both continuous distributed deformation and strain localisation along large-scale faults (Wright et al., 2026). Geodetic strain rate mapping shows that, in the plateau interior, extension outpaces convergence south of the Kunlun fault, producing dilatation in the central plateau. High strain rates are focused on major strike-slip systems such as the Kunlun and Xianshuihe faults (Wright et al., 2026), and along large N-S trending rifts (Armijo et al., 1986), including the Yadong-Gulu and Pumqu-Xainza rifting systems (Chen et al., 2024). Overall, the plateau's present-day tectonics are dominated by strike-slip faulting with minor normal-faulting (Elliott et al., 2010).

Although less frequent and generally lower in magnitude, normal-faulting earthquakes in Tibet are not uncommon. Extensional faulting is estimated to release nearly 20% of the total extensional strain across the Plateau (Elliott et al., 2010). Recent normal-faulting earthquakes clearly linked to specific rift systems include the Damxung event (Bie et al., 2014) and the Nima (Ryder et al., 2010) and Zhongba earthquake sequences (Ryder et al., 2012), among others. Focusing on the Pumqu-Xainza Rift (PXR), a sequence of Mw 5.7-6.2 earthquakes struck the northern part of the system in the 1990s (Wang et al., 2014).

The 2020 earthquake occurred in an area lacking field-mapped faults; notably, even the large 2025 event ruptured a previously undocumented fault system. Aftershock

ORIGINAL UNEDITED MANUSCRIPT

Downloaded from academic.oup.com/gji/advance-article/doi/10.1093/gji/ggag516/9121041 by East Anglia University user on 24 November 2026

relocations following the 2020 earthquake (Zhang et al., 2020) delineate a NW-SE trending normal fault (Figure 1). A topographic profile perpendicular to the inferred fault trace reveals elevation variations that are inconsistent with the typical surface geomorphology of normal faults: the hanging wall side stands lower than the footwall side. This suggests that active normal-faulting is not clearly expressed in surface topography. These observations raise questions about the role that moderate-magnitude earthquakes play in shaping surface geomorphology.

3. Data and method

Sentinel-1 satellites provide ascending and descending observations covering the Dingri area in Tibet. We generate co- and post-seismic interferograms using the open-source GMTSAR software package (Sandwell et al., 2011). Topographic phase is removed using the 90-m Shuttle Radar Topography Mission (SRTM) digital elevation model (Farr et al., 2007). Interferometric phase is unwrapped using SNAPHU – the Statistical-Cost, Network-Flow Algorithm for Phase Unwrapping (Chen & Zebker, 2000). We then apply a joint deramp and atmospheric noise correction to the interferograms (Bie et al., 2014). The co- and post-seismic interferogram pairs used are summarised in Table S1.

We also exploit the numerous pre-processed interferograms archived in the COMET-LiCSAR portal (Lazecký et al., 2020). We construct a ~5-year postseismic deformation time series from the descending and ascending interferogram networks (Figure S1) using the LiCSBAS package (Morishita et al., 2020).

ORIGINAL UNEDITED MANUSCRIPT

Downloaded from academic.oup.com/gji/advance-article/doi/10.1093/gji/ggag516/9121041 by East Anglia University user on 24 November 2026

To compute PCMR, we first invert for co- and post-seismic distributed slip, following established procedures (e.g., Bie et al., 2014; Bie et al., 2017; Kufner et al., 2023). Earthquake source parameters are explored via Bayesian inversion of downsampled coseismic interferograms (Bagnardi & Hooper, 2018), assuming a uniform dislocation in an elastic half-space (Okada 1985). Distributed slip models are then derived by least-squares inversion on an extended fault plane. Afterslip models are obtained at selected epochs from the cumulative postseismic deformation – approximately one and five years after the 2020 mainshock. We derive slip errors by inverting 100 sets of synthetic noise-perturbed displacements and computing standard deviations of slip values for each fault patch (Bie et al., 2014).

4. Results

4.1. Co- and post-seismic displacements

Figure 2 presents the co- and post-seismic interferograms for the 2020 Mw 5.6 Dingri earthquake. The maximum line-of-sight (LOS) displacement reaches ~15 cm in the direction away from the satellite. Dense fringes are clearly visible in both viewing geometries at approximately the same location, indicating that motion on the fault is dominated by dip-slip.

Postseismic interferograms exhibit generally good coherence, even for the pair with a 5-year temporal baseline, largely due to the semi-arid conditions and sparsely vegetated terrain. To minimise potential seasonal hydrological effects, we form interferograms from images acquired in the same season, which also help to maintain coherence. On the ascending track, the one-year postseismic interferogram shows ~5

ORIGINAL UNEDITED MANUSCRIPT

Downloaded from academic.oup.com/gji/advance-article/doi/10.1093/gji/ggag516/9121041 by East Anglia University user on 24 November 2026

cm of LOS displacement. The amplitude increases to ~6 cm in the 5-year postseismic interferogram. The change reveals a non-linear decrease in the displacement rate. A similar trend can be inferred from the descending interferograms (Figure 2). The postseismic deformation time-series generated with LiCSBAS are shown in Figure S2. Logarithmic fits to the deformation time series of selected pixels confirm a non-linear decay of the deformation rate.

We note that postseismic displacements on both sides of the fault are in the same LOS direction as in the coseismic interferograms (Figure 2), suggesting that continued slip on the fault plane dominates near-field postseismic deformation. The step change across the fault trace further implies that shallow afterslip may have reached the surface.

4.2. Co- and post-seismic distributed slip model

Table 1 summarises the fault geometry and source parameters from the uniform slip modelling. Parameter uncertainties and trade-offs are shown in Figure S3. The fault plane strikes NW-SE, consistent with the aftershock distribution, dips to the NE, and has a rake of approximately -90°. The epicentre inferred from the InSAR inversion lies ~10 km NE of the USGS location and ~16 km north of the GCMT solution. Normal slip component dominates the distributed slip (Figure 3a), as revealed by the uniform slip model. Most slip is concentrated at shallow depths of 2–6 km, with a maximum of 0.8 m at ~3.5 km depth. The geodetic moment release is 3.62×10^{17} Nm, equivalent to Mw 5.64. The distributed coseismic slip exhibits an overall quasi-circular pattern.

The two afterslip models display a consistent spatial pattern. The principal afterslip patches are at 1–4 km depth and form an elliptical zone whose long axis aligns with

ORIGINAL UNEDITED MANUSCRIPT

Downloaded from academic.oup.com/gji/advance-article/doi/10.1093/gji/ggag516/9121041 by East Anglia University user on 24 November 2026

the oblique afterslip direction. The maximum afterslip is located at 2.5 km depth, outside of the 0.6 m coseismic slip contour. Afterslip partially overlaps the coseismic slip but is, overall, shallower and distributed around the maximum coseismic slip patch (Figure 3). The maximum cumulative afterslip increases from ~0.2 m at one year to ~0.3 m at five years after the earthquake. The difference in afterlip amplitude is shown Figure S4. The five-year cumulative afterslip moment is 2.05×10^{17} Nm, equivalent to a Mw 5.47 earthquake. This amounts to 56.6% of the coseismic moment release.

The coseismic slip standard deviation is generally < 2 cm. The afterslip models show slightly larger standard deviations, but these remain < 4 cm. The patches with the largest standard deviations appear at depths > 5 km, deeper than the area where the largest afterslip is concentrated on the fault (Figure S5). Our slip models reproduce the observed displacements well (Figure 4, 5 and S6). We note that the PCMR reported here is a lower bound. The coseismic slip model is inverted from interferograms that contain early afterslip – for example, the descending pair 20200316-20200328 (Figure 2) includes eight days of afterslip. Although the secondary SAR acquisition for the ascending interferogram occurred on the day of mainshock, it still captures the very earliest afterslip immediately following earthquake rupture. Conversely, the postseismic observations miss the afterslip that occurred between the earthquake and the first postseismic SAR acquisitions, resulting in an underestimated afterslip moment. Both effects lead to an underestimated PCMR.

5. Discussion

5.1. Pronounced afterslip moment release

ORIGINAL UNEDITED MANUSCRIPT

Downloaded from academic.oup.com/gji/advance-article/doi/10.1093/gji/ggag516/9121041 by East Anglia University user on 24 November 2026

Postseismic displacements and afterslip modelling clearly indicate that postseismic moment release increases with time. Five years after the 2020 earthquake, the cumulative afterslip moment is 2.1×10^{17} Nm, equivalent to 56.6% of the coseismic moment release, compared with 1.8×10^{17} Nm one year after the earthquake. In our compilation (Figure 6), this ratio is higher than for all other normal-faulting earthquakes, despite its comparatively modest magnitude. The only other moderate earthquake with a postseismic moment exceeding half of the coseismic moment is the 1999 Mw 5.9 Athens earthquake in Greece (Atzori et al., 2008). For larger ($M > 6$) normal-faulting events, the ratio typically ranges from a few percents to < 50%, broadly consistent with previous estimates across faulting mechanisms (e.g., Fattahi et al., 2015; Hawthorne et al., 2016; Wimpenny et al., 2017; Churchill et al., 2022).

InSAR and GNSS studies of moderate-magnitude ($M < 6$) earthquakes are relatively uncommon, likely because their lower signal-to-noise ratios make it difficult to place robust constraints on both co- and post-seismic slip. Using borehole strainmeter data, Hawthorne et al. (2016) showed that the ratio of postseismic to coseismic moment following M 1.9–5 earthquakes in California can be up to four times higher than for most $M > 6$ earthquakes in their compilation. Although a simple linear relationship between the moment ratio with magnitude is not evident, a clear difference emerges between small and large earthquakes.

What controls the PCMR remains under debate. A particular important observation is that, for earthquakes of similar magnitude, PCMR can vary significantly. For example, the Mw 6.3 Thessaly, Greece earthquake has a ratio of 7.8% (Tolomei et al., 2025), far lower than other Mw 6.3 earthquakes compiled here (Figure 6; Table S2). Churchill et

ORIGINAL UNEDITED MANUSCRIPT

Downloaded from academic.oup.com/gji/advance-article/doi/10.1093/gji/ggag516/9121041 by East Anglia University user on 24 November 2026

al. (2022) explored a wide range of potential controls on PCMR, including mainshock characteristics, fault and regional kinematics, and observational factors (e.g., data coverage and modelling approaches). For Mw > 6 earthquakes, they found that PCMR is not primarily controlled by faulting mechanism or depth; instead, higher fault slip rates and lower rupture aspect ratios (i.e., more compact ruptures) tend to be associated with higher PCMR.

Fault slip rate is often used as a proxy for fault maturity, which likely contributes to PCMR variability, particularly in endmember cases with high PCMR. Afterslip moment releases for the 2004 Mw 6.0 Parkfield and 2008 Mw 6.8 Methoni earthquakes exceed their coseismic moments, and both faults have high slip rates and strongly localised strain rates. Similarly, localised high dilatational (~50 – 150 nstrain/yr) strain rates (Wright et al., 2026; Chen et al., 2024) and fault slip rates of >2 mm/yr (Ma et al., 2026) are observed in the southern PXR, where the 2020 Dingri earthquake occurred. Following this logic, one might expect a high, rather than moderate (14.2% as reported by He et al., 2025), PCMR for the 2025 Mw 7.1 Dingri earthquake in the same region that mainly ruptured an active normal fault dipping to the west and forming a conjugate structure with the 2020 earthquake fault (Ma et al., 2026). This apparent mismatch may indicate that the faults that ruptured in these two events accommodate extension differently, with the 2020 Dingri fault segment more prone to aseismic slip in the interseismic period.

Within the rate-and-state frictional framework, afterslip is favoured on frictionally stable portions of the fault where the depth-dependent parameter (a-b) > 0 (Marone et al., 1991; Perfettini & Avouac, 2004). Churchill et al. (2022) hypothesised that low-

ORIGINAL UNEDITED MANUSCRIPT

Downloaded from academic.oup.com/gji/advance-article/doi/10.1093/gji/ggag516/9121041 by East Anglia University user on 24 November 2026

dip faults may permit more afterslip by providing a larger unruptured area in stable or conditionally stable regimes. This hypothesis is worth investigating by comparing the Dingri and Magna cases: the 2020 Mw 5.7 Magna, Utah earthquake ruptured a shallow-dipping (30–35°) fault (Pang et al., 2020), yet the afterslip moment and PCMR are not explicitly reported (Pollitz et al., 2021). Another hypothesis is that, if (a – b) is primarily depth-controlled, shallower earthquakes may permit proportionally more downdip afterslip and thus a higher overall PCMR. Our observations do not fully support this: the Dingri earthquake triggered afterslip mostly updip of the main rupture, although the primary co-seismic slip patches are at shallow depths (2–6 km). On the other hand, the 1999 Mw 5.9 Athens earthquake triggered afterslip slightly deeper than the main slip patches (Atzori et al, 2008), which may point to lithological and thermal contrasts between the two faults.

The 2020 Dingri earthquake occurred near the Lhagoi Kangri gneiss dome, where the Triassic siliciclastic sedimentary layer is inferred to be ≥3 km thick (Diedesch et al., 2016). Siliciclastic sedimentary rocks are generally velocity-strengthening (Silva et al., 2024), making them prone to aseismic slip. Most afterslip following the Dingri earthquake lies within this sedimentary section and extends deeper towards the southern end of the fault. While frictional properties are largely depth- and temperature-dependent, along-strike heterogeneity is well recognised (e.g., Lay and Nishenko 2022), and attributed to variations in environmental conditions such as lithology, presence of fluids and fault roughness (Eijsink et al., 2025). Such heterogeneity could explain deep afterslip coincident with coseismic slip. We also note that coseismic slip partially overlaps with afterslip in the sedimentary layer. Although earthquakes do not nucleate in the velocity-strengthening regions, rupture can

ORIGINAL UNEDITED MANUSCRIPT

Downloaded from academic.oup.com/gji/advance-article/doi/10.1093/gji/ggag516/9121041 by East Anglia University user on 24 November 2026

propagate into nearby stable areas (e.g., the sedimentary layer) via dynamic weakening (Noda and Lapusta, 2013). To better resolve spatial variations in fault friction, a detailed assessment of interseismic coupling is needed to delineate asperities (seismogenic) and creeping sections (aseismic) on the fault system in the Dingri area.

5.2. Implications on earthquake hazard in the region

As shown by the topographic profile perpendicular to the fault trace (Figure 1), the hanging wall side stands higher than the footwall. This surface expression complicates the identification of active normal faults based solely on geomorphology. A similar situation exists in the 1990s earthquake sequence in the northern PXR (Wang et al., 2014), where active faulting is not clearly expressed in surface topography. Elastic dislocation modelling would predict hanging wall subsidence for a rupture that reaches the surface. If the 2020 Mw 5.6 Dingri earthquake contributes to building topography relief, one would expect a low-relief graben or half-graben east of the fault trace. The absence of such structures may indicate that moderate-magnitude earthquakes contribute little, if at all, to building topographic relief that is indicative of active faulting.

The normal fault that ruptured in 2020 may be structurally linked to the eastward-dipping secondary fault that slipped in the 2025 earthquake (Figure 1). Compared with the westward-dipping fault that hosted the main 2025 rupture, the eastward-dipping fault shows no clear topographic step (Qiao et al., 2025). Nevertheless, its potential to rupture is evident – from the 2020 earthquake and triggered slip in 2025. It is reasonable to speculate that, prior to 2020, both eastward- and westward-dipping

ORIGINAL UNEDITED MANUSCRIPT

Downloaded from academic.oup.com/gji/advance-article/doi/10.1093/gji/ggag516/9121041 by East Anglia University user on 24 November 2026

faults in the Dingri region had accumulated sufficient extensional stress to rupture. The remaining question is how the conjugate pair accommodates the E-W extension. Chen et al. (2024) proposed elastic dislocation models with conjugate structures slipping at 1-2 mm/yr in southern Tibet. The broader zone of high dilatational strain rate in the Dingri region (Wright et al., 2026) may require even higher fault slip rates, consistent with the link between high PCMR and slip rate discussed in Section 5.1. Whether the conjugate faults accommodate strain equally or disproportionally remain to be resolved.

6. Conclusions

In this study, we resolved the co- and post-seismic deformation of the 2020 Mw 5.6 Dingri earthquake from InSAR observations, and derived kinematic slip models. Coseismic slip is concentrated in shallow, elliptical patches dominated by normal-faulting at ~2–6 km depth, whereas afterslip is distributed at ~1–4 km that decays nonlinearly in time. The five-year cumulative afterslip moment is 2.1×10^{17} Nm, equivalent to 56.6% of the coseismic moment, placing this event among the highest PCMR values reported for normal-faulting earthquakes of this size. The near-fault step, shared LOS polarity with the coseismic field, and logarithmic-like decay favour continued slip on the fault plane within velocity-strengthening materials. The lithological context near the Lhagoi Kangri gneiss dome, including a ≥3 km siliciclastic sedimentary cover, together with localised high strain rate in the southern PXR, plausibly promotes shallow aseismic slip and helps explain the elevated PCMR. These estimates are likely lower bounds, as early afterslip partly contaminates the coseismic interferograms and is partially missed in the earliest postseismic period. Our results

ORIGINAL UNEDITED MANUSCRIPT

Downloaded from academic.oup.com/gji/advance-article/doi/10.1093/gji/ggag516/9121041 by East Anglia University user on 24 November 2026

also highlight the challenge of identifying active normal faults where geomorphic expression is weak, and underscore the value of interseismic coupling analyses to map asperities and creeping sections, and to assess strain partitioning on conjugate normal faults.

Acknowledgements

Lidong Bie thanks Yukitoshi Fukahata for valuable discussions during the preparation of this study. Conor Rutland acknowledges the PhD studentship funded by the Faculty of Science at the University of East Anglia. We thank the editor, Dr Kosuke Heki, reviewer Mikhail Rodkin, and the anonymous reviewer for their constructive comments.

Data availability

Sentinel-1 SAR images are sourced from the European Space Agency (https://browser.dataspace.copernicus.eu). The postseismic interferograms are available from LiCSAR portal (Lazecký et al., 2020). LiCSBAS (Morishita et al., 2020) is used for postseismic deformation time-series construction. Some maps in this study were created using Generic Mapping Tools (GMT) (Wessel et al., 2019).

ORIGINAL UNEDITED MANUSCRIPT

Downloaded from academic.oup.com/gji/advance-article/doi/10.1093/gji/ggag516/9121041 by East Anglia University user on 24 November 2026

References

Alwahedi, M.A. and Hawthorne, J.C., 2019. Intermediate-magnitude postseismic slip follows intermediate-magnitude (M 4 to 5) earthquakes in California. *Geophysical Research Letters*, *46*(7), pp.3676-3687.

Armijo, R., Tapponnier, P., Mercier, J.L. and Han, T.L., 1986. Quaternary extension in southern Tibet: Field observations and tectonic implications. *Journal of Geophysical Research: Solid Earth*, *91*(B14), pp.13803-13872.

Atzori, S., Manunta, M., Fornaro, G., Ganas, A. and Salvi, S., 2008. Postseismic displacement of the 1999 Athens earthquake retrieved by the Differential Interferometry by Synthetic Aperture Radar time series. *Journal of Geophysical Research: Solid Earth*, *113*(B9).

Bagnardi, M. and Hooper, A., 2018. Inversion of surface deformation data for rapid estimates of source parameters and uncertainties: A Bayesian approach. *Geochemistry, Geophysics, Geosystems*, *19*(7), pp.2194-2211.

Bie, L., Ryder, I., Nippress, S.E. and Bürgmann, R., 2014. Coseismic and post-seismic activity associated with the 2008 M w 6.3 Damxung earthquake, Tibet, constrained by InSAR. *Geophysical Journal International*, *196*(2), pp.788-803.

Bie, L., González, P.J. and Rietbrock, A., 2017. Slip distribution of the 2015 Lefkada earthquake and its implications for fault segmentation. *Geophysical Journal International*, *210*(1), pp.420-427.

Bürgmann, R. and Dresen, G., 2008. Rheology of the lower crust and upper mantle: Evidence from rock mechanics, geodesy, and field observations. *Annu. Rev. Earth Planet. Sci.*, *36*(1), pp.531-567.

Chen, C. W., and H. A. Zebker (2000), Network approaches to two-dimensional phase unwrapping: Intractability and two new algorithms, J. Op. Soc. Am. A Op., Image Sci., 17(3), 401–414, doi:10.1364/JOSAA.17.000401.

Chen, H., Qu, C., Zhao, D., Shan, X., Li, C. and Dal Zilio, L., 2024. Large-scale extensional strain in Southern Tibet from Sentinel-1 InSAR and GNSS data. *Geophysical Research Letters*, *51*(19), p.e2024GL110512.

Downloaded from academic.oup.com/gji/advance-article/doi/10.1093/gji/ggag516/9121041 by East Anglia University user on 24 November 2026

ORIGINAL UNEDITED MANUSCRIPT

Chen, T. and Lapusta, N., 2009. Scaling of small repeating earthquakes explained by interaction of seismic and aseismic slip in a rate and state fault model. *Journal of Geophysical Research: Solid Earth*, *114*(B1).

Churchill, R.M., Werner, M.J., Biggs, J. and Fagereng, Å., 2022. Afterslip moment scaling and variability from a global compilation of estimates. *Journal of Geophysical Research: Solid Earth*, *127*(4), p.e2021JB023897.

D'Agostino, N., Cheloni, D., Fornaro, G., Giuliani, R. and Reale, D., 2012. Space-time distribution of afterslip following the 2009 l'aquila earthquake. Journal of Geophysical Research, 117(B2), B02402.

Diedesch, T.F., Jessup, M.J., Cottle, J.M. and Zeng, L., 2016. Tectonic evolution of the middle crust in southern Tibet from structural and kinematic studies in the Lhagoi Kangri gneiss dome. Lithosphere, 8(5), pp.480-504.

Eijsink, A., Wood, C., Marone, C., Shokouhi, P., Rivière, J. and Elsworth, D., 2025. Evolution of frictional properties, permeability and elastic parameters due to surface roughness changes during fault maturation in laboratory shear experiments. Earth and Planetary Science Letters, 671, p.119684.

Elliott, J.R., Walters, R.J., England, P.C., Jackson, J.A., Li, Z. and Parsons, B., 2010. Extension on the Tibetan plateau: recent normal faulting measured by InSAR and body wave seismology. *Geophysical Journal International*, *183*(2), pp.503-535.

Farr, T. G., E. Rodriguez (2007), The shuttle radar topography mission, Rev. Geophys., 45(2), doi:10.1029/2005RG000183.

Fattahi, H., Amelung, F., Chaussard, E. and Wdowinski, S., 2015. Coseismic and postseismic deformation due to the 2007 M5. 5 Ghazaband fault earthquake, Balochistan, Pakistan. *Geophysical Research Letters*, *42*(9), pp.3305-3312.

Hamiel, Y., Baer, G., Kalindekafe, L., Dombola, K. and Chindandali, P., 2012. Seismic and aseismic slip evolution and deformation associated with the 2009–2010 northern Malawi earthquake swarm, east african rift. Geophysical Journal International, 191(3), 898–908.

ORIGINAL UNEDITED MANUSCRIPT

Downloaded from academic.oup.com/gji/advance-article/doi/10.1093/gji/ggag516/9121041 by East Anglia University user on 24 November 2026

Hawthorne, J.C., Simons, M. and Ampuero, J.P., 2016. Estimates of aseismic slip associated with small earthquakes near San Juan Bautista, CA. *Journal of Geophysical Research: Solid Earth*, *121*(11), pp.8254-8275.

He, K., Cai, J., Wen, Y. and Xu, C., 2026. Bipartite rupture in the 2025 Dingri earthquake indicates normal conjugate faulting during orogenic collapse. *Communications Earth & Environment*.

He, L., Feng, G., Jiang, H., Wang, W., Liu, X., Wang, Y. and Yun, S.-H., 2025. Coseismic kinematics and early afterslip evolution of the 2025 Mw 7.1 Dingri earthquake (southern Tibet) from space geodesy. Geophysical Research Letters, 52, e2025GL118937.

Hong, S., Liu, M., Zhou, X., Meng, G. and Dong, Y., 2023. Afterslip on conjugate faults of the 2020 M W 6.3 Nima Earthquake in the Central Tibetan Plateau: Evidence from InSAR measurements. Bulletin of the Seismological Society of America, 113(5), pp.2026-2040.

Kufner, S.K., Bie, L., Gao, Y., Lindner, M., Waizy, H., Kakar, N. and Rietbrock, A., 2023. The devastating 2022 M6. 2 Afghanistan earthquake: Challenges, processes, and implications. *Geophysical Research Letters*, *50*(11), p.e2022GL102176.

Lay, T. and Nishenko, S.P., 2022. Updated concepts of seismic gaps and asperities to assess great earthquake hazard along South America. Proceedings of the National Academy of Sciences, 119(51), p.e2216843119.

Lazecký, M., Spaans, K., González, P.J., Maghsoudi, Y., Morishita, Y., Albino, F., Elliott, J., Greenall, N., Hatton, E., Hooper, A. and Juncu, D., 2020. LiCSAR: An automatic InSAR tool for measuring and monitoring tectonic and volcanic activity. *Remote Sensing*, *12*(15), p.2430.

Ma, Z., Li, C., Zeng, H., Chen, H., Lyu, M., Zhang, Y., Dal Zilio, L., Shan, X. and Wei, S., 2026. Deciphering stress perturbations throughout the 2025 M w 7.1 Dingri, Southern Xizang Earthquake. *Nature Communications*.

Marone, C., Scholtz, C., & Bilham, R. (1991). On the mechanics of earthquake afterslip. Journal of Geophysical Research, 96(B5), 8441–8452. https://doi.org/10.1029/91jb00275

ORIGINAL UNEDITED MANUSCRIPT

Downloaded from academic.oup.com/gji/advance-article/doi/10.1093/gji/ggag516/9121041 by East Anglia University user on 24 November 2026

Morishita, Y., Lazecky, M., Wright, T.J., Weiss, J.R., Elliott, J.R. and Hooper, A., 2020. LiCSBAS: An open-source InSAR time series analysis package integrated with the LiCSAR automated Sentinel-1 InSAR processor. *Remote Sensing*, *12*(3), p.424.

Noda, H. and Lapusta, N., 2013. Stable creeping fault segments can become destructive as a result of dynamic weakening. Nature, 493(7433), pp.518-521.

Okada, Y., 1985. Surface deformation due to shear and tensile faults in a half-space. *Bull. Seismol. Soc. Am*, *75*(4), pp.1135-1154.

Pang, G., Koper, K.D., Mesimeri, M., Pankow, K.L., Baker, B., Farrell, J., Holt, J., Hale, J.M., Roberson, P., Burlacu, R. and Pechmann, J.C., 2020. Seismic analysis of the 2020 Magna, Utah, earthquake sequence: Evidence for a listric Wasatch fault. Geophysical Research Letters, 47(18), p.e2020GL089798.

Perfettini, H., & Avouac, J.-P. (2004). Postseismic relaxation driven by brittle creep: A possible mechanism to reconcile geodetic measurements and the decay rate of aftershocks, application to the chi-chi earthquake, taiwan. Journal of Geophysical Research, 109,B02304. https://doi.org/10.1029/2003jb002488

Pollitz, F.F., Wicks, C.W. and Svarc, J.L., 2021. Coseismic fault slip and afterslip associated with the 18 March 2020 M 5.7 Magna, Utah, earthquake. Seismological Society of America, 92(2A), pp.741-754.

Pousse-Beltran, L., Socquet, A., Benedetti, L., Doin, M.-P., Rizza, M. and D'Agostino, N., 2020. Localized afterslip at geometrical complexities revealed by InSAR after the 2016 Central Italy seismic sequence. Journal of Geophysical Research: Solid Earth, 125, e2019JB019065. https://doi.org/10.1029/2019JB019065

Qiao, X., Lu, Z., Yan, S., Shi, H., Zhi, M. and Zhao, D., 2025. The 2025 Mw7. 0 Dingri earthquake: Conjugate normal faulting of a graben structure in the southern Xainza-Dinggye rift. *Geophysical Research Letters*, *52*(12), p.e2025GL116154.

Riva, R., Borghi, A., Aoudia, A., Barzaghi, R., Sabadini, R. and Panza, G., 2007. Viscoelastic relaxation and long-lasting after-slip following the 1997 umbria-marche (central Italy) earthquakes. Geophysical Journal International, 169(2), 534–546. https://doi.org/10.1111/j.1365-246x.2007.03315.x

ORIGINAL UNEDITED MANUSCRIPT

Downloaded from academic.oup.com/gji/advance-article/doi/10.1093/gji/ggag516/9121041 by East Anglia University user on 24 November 2026

Ryder, I., Bürgmann, R. and Fielding, E., 2012. Static stress interactions in extensional earthquake sequences: An example from the South Lunggar Rift, Tibet. *Journal of Geophysical Research: Solid Earth*, *117*(B9).

Ryder, I., Bürgmann, R. and Sun, J., 2010. Tandem afterslip on connected fault planes following the 2008 Nima-Gaize (Tibet) earthquake. *Journal of Geophysical Research: Solid Earth*, *115*(B3).

Sandwell, D., R. Mellors, X. Tong, M. Wei, and P. Wessel (2011), Open radar interferometry software for mapping surface deformation, Eos Trans. AGU, 92(28), 234, doi:10.1029/2011EO280002.

Silva, D.C.A., Skurtveit, E., Soldal, M. and Braathen, A., 2024. Frictional strength of siliciclastic sediment mixtures in fault stability assessment. Journal of Structural Geology, 187, p.105232.

Tolomei, C., Ganas, A., Bignami, C., Atzori, S., Foumelis, M. and Konstantakopoulou, E., 2025. Two phases of aseismic afterslip following the March 2021 Damasi, Greece, normal faulting earthquakes retrieved from InSAR measurements. *Scientific Reports*, *15*(1), p.12995.

Wang, H., Elliott, J.R., Craig, T.J., Wright, T.J., Liu-Zeng, J. and Hooper, A., 2014. Normal faulting sequence in the Pumqu-Xainza Rift constrained by InSAR and teleseismic body-wave seismology. *Geochemistry, Geophysics, Geosystems*, *15*(7), pp.2947-2963.

Wessel, P., Luis, J.F., Uieda, L.A., Scharroo, R., Wobbe, F., Smith, W.H. and Tian, D., 2019. The generic mapping tools version 6. *Geochemistry, Geophysics, Geosystems*, *20*(11), pp.5556-5564.

Wimpenny, S., Copley, A. and Ingleby, T., 2017. Fault mechanics and post-seismic deformation at Bam, SE Iran. *Geophysical Journal International*, *209*(2), pp.1018-1035.

Wright, T.J., Elliott, J.R., Wang, H. and Ryder, I., 2013. Earthquake cycle deformation and the Moho: Implications for the rheology of continental lithosphere. *Tectonophysics*, *609*, pp.504-523.

Wright, T.J., Houseman, G.A., Fang, J., Maghsoudi, Y., Hooper, A.J., Elliott, J.R., Evans, L., Lazecky, M., Ou, Q., Parsons, B.E. and Rollins, J.C., 2026. High-resolution geodetic velocities reveal role of weak faults in deformation of Tibetan Plateau. *Science*, *391*(6784), pp.499-503.

Zhang, X., Jiang X., Xue, Y., Yao, Q., Xie, M., Zhang, Y., Song, J., Lu, X., Yu, C., Fan, Z. and Tian, L., 2020. Summary of the Dingri Ms 5.9 earthquake in Tibet on March 20, 2020. Seismological and

Downloaded from academic.oup.com/gji/advance-article/doi/10.1093/gji/ggag516/9121041 by East Anglia University user on 24 November 2026

ORIGINAL UNEDITED MANUSCRIPT

449 Geomagnetic Observation and Research (in Chinese), 41(4): 193-203. doi: 10.3969/j.issn.1003-3246.
450 2020.04.024

451

Downloaded from academic.oup.com/gji/advance-article/doi/10.1093/gji/ggag516/9121041 by East Anglia University user on 24 November 2026

ORIGINAL UNEDITED MANUSCRIPT

Figure 1. (a) Tectonic map of the Dingri region in southern Tibet. Focal mechanisms for the Mw 5.6 Dingri earthquake are shown in red at locations reported by the USGS and GCMT. Focal mechanism for the 2025 Mw 7.1 Dingri earthquake is from GCMT and shown in blue. Oranges dots show relocated aftershocks following the 2020 earthquake (Zhang et al., 2020). Blue lines depict fault traces of the 2025 Mw 7.1 Dingri earthquake (Ma et al., 2026). The red line indicates the fault surface trace determined for the 2020 earthquake in this study. (b) Topographic profile perpendicular to the fault trace. The red line shows the NE-dipping fault that ruptured during the 2020 Mw 5.6 earthquake.

Figure 2. Co- and post-seismic interferograms for the 2020 Mw 5.6 Dingri earthquake. Date pairs in each subfigure indicate when the images used for interferometry were acquired.

Figure 3. (a) Coseismic distributed slip model for the 2020 Mw 5.6 Dingri earthquake. (b) Afterslip distribution ~1 year after the earthquake. (c) Afterslip distribution ~5 years after the earthquake. Coseismic slip contours are shown in the afterslip models for comparison. Note the different colour scales for the coseismic slip and afterslip models.

Figure 4. Coseismic displacement observations, downsampled data, model predictions, and residuals for the ascending track (upper panel) and descending track (lower panel). The black dashed line shows the fault trace determined from uniform-slip modelling in this study.

Figure 5. Same as Figure 4, but for the cumulative ~5 years of postseismic displacement.

Figure 6. Compilation of postseismic-to-coseismic moment ratio (PCMR) determined by geodetic studies of normal-faulting earthquakes (Table S2). The 2020 Mw 5.6 Dingri earthquake stands out as having the highest PCMR.

ORIGINAL UNEDITED MANUSCRIPT

Downloaded from academic.oup.com/gji/advance-article/doi/10.1093/gji/ggag516/9121041 by East Anglia University user on 24 November 2026

473 Table 1. Fault geometry and source parameters derived from Bayesian inversion, assuming
474 uniform slip on a fault plane buried in an elastic half-space. GCMT and USGS solutions for the
475 2020 Mw 5.6 earthquake are also included for comparison. The reference point is (87.387°,
476 28.666°).

477

ORIGINAL UNEDITED MANUSCRIPT

Downloaded from academic.oup.com/gji/advance-article/doi/10.1093/gji/ggag516/9121041 by East Anglia University user on 24 November 2026

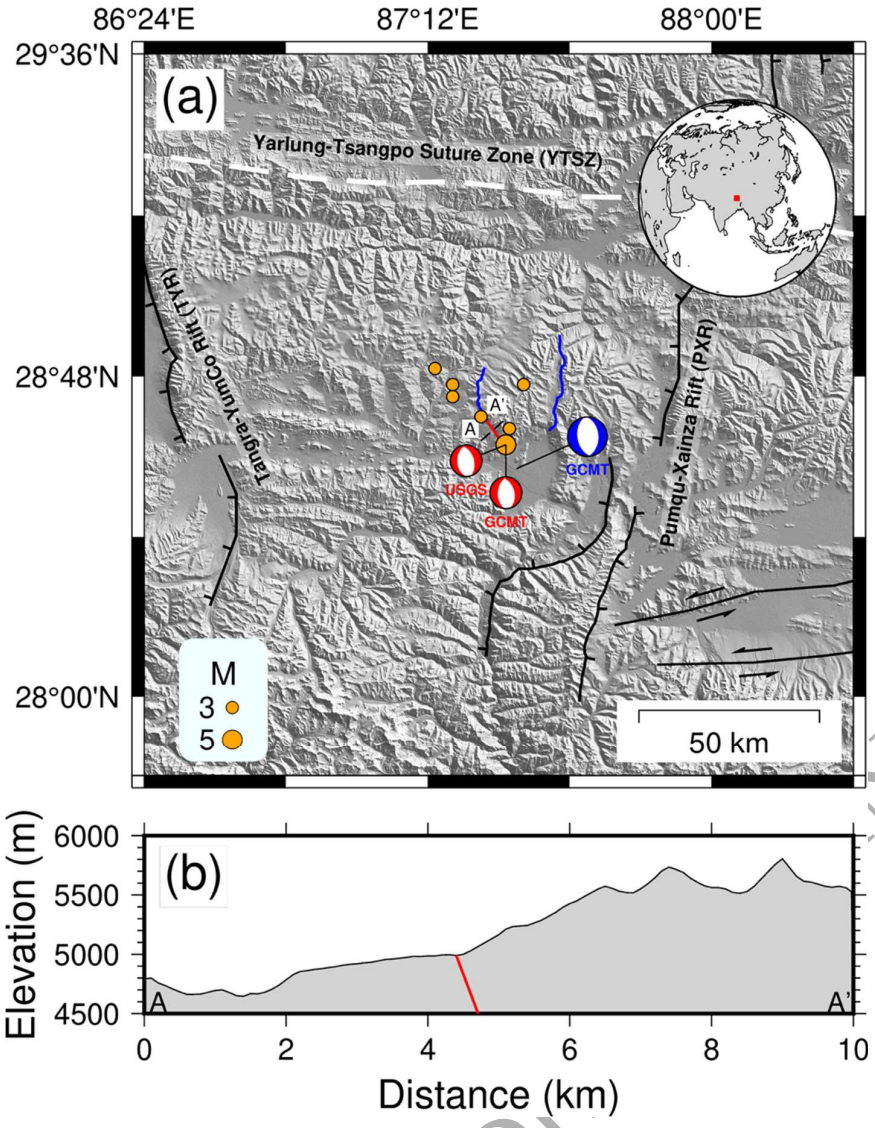

478

479 Figure 1. (a) Tectonic map of the Dingri region in southern Tibet. Focal mechanisms for the
480 Mw 5.6 Dingri earthquake are shown in red at locations reported by the USGS and GCMT.
481 Focal mechanism for the 2025 Mw 7.1 Dingri earthquake is from GCMT and shown in blue.
482 Oranges dots show relocated aftershocks following the 2020 earthquake (Zhang et al., 2020).
483 Blue lines depict fault traces of the 2025 Mw 7.1 Dingri earthquake (Ma et al., 2026). The red
484 line indicates the fault surface trace determined for the 2020 earthquake in this study. (b)
485 Topographic profile perpendicular to the fault trace. The red line shows the NE-dipping fault
486 that ruptured during the 2020 Mw 5.6 earthquake.

ORIGINAL UNEDITED MANUSCRIPT

Downloaded from academic.oup.com/gji/advance-article/doi/10.1093/gji/ggag516/9121041 by East Anglia University user on 24 November 2026

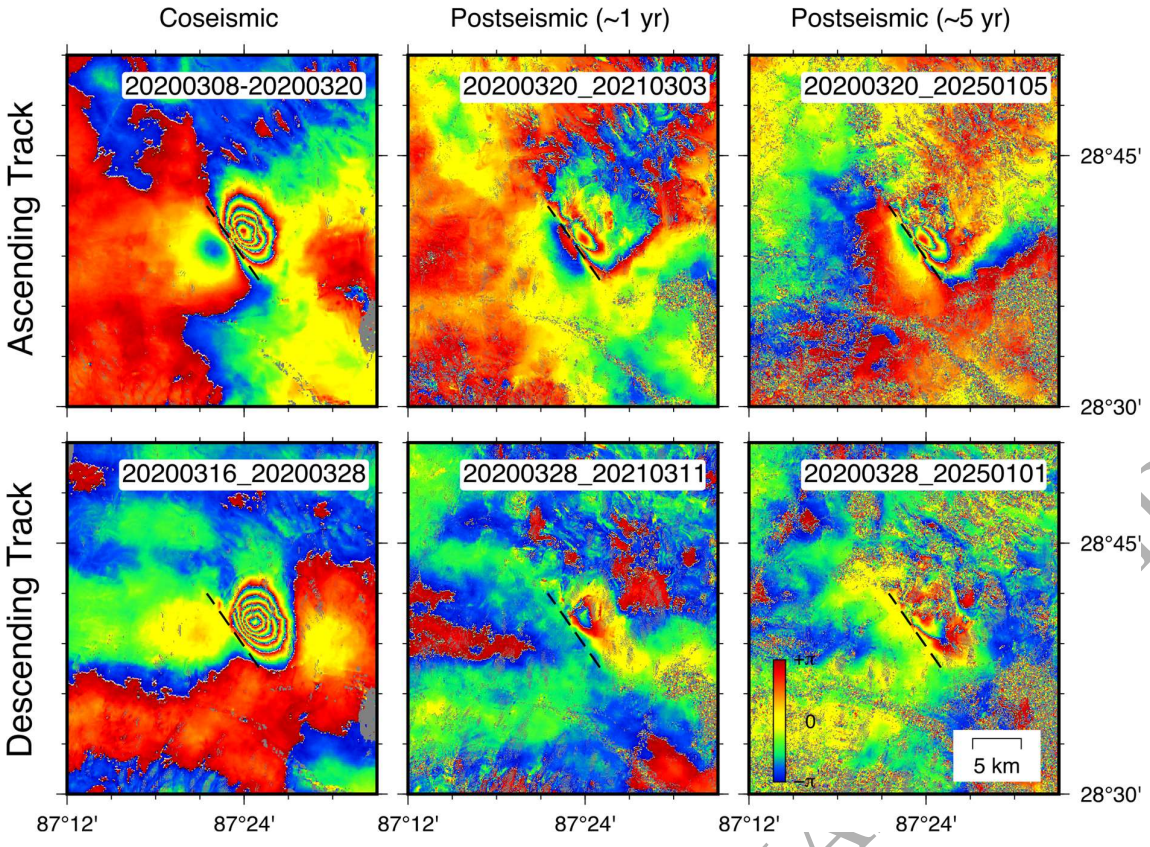

487

488 Figure 2. Co- and post-seismic interferograms for the 2020 Mw 5.6 Dingri earthquake. Date

489 pairs in each subfigure indicate when the images used for interferometry were acquired.

490

ORIGINAL UNEDITED MANUSCRIPT

Downloaded from academic.oup.com/gji/advance-article/doi/10.1093/gji/ggag516/9121041 by East Anglia University user on 24 November 2026

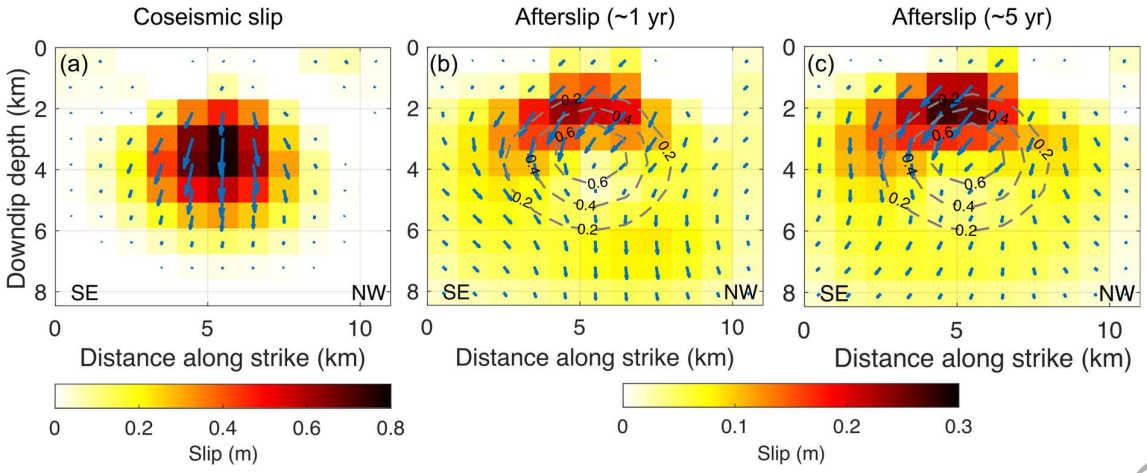

491

492 Figure 3. (a) Coseismic distributed slip model for the 2020 Mw 5.6 Dingri earthquake. (b)

493 Afterslip distribution ~1 year after the earthquake. (c) Afterslip distribution ~5 years after the

494 earthquake. Coseismic slip contours are shown in the afterslip models for comparison. Note

495 the different colour scales for the coseismic slip and afterslip models.

496

ORIGINAL UNEDITED MANUSCRIPT

Downloaded from academic.oup.com/gji/advance-article/doi/10.1093/gji/ggag516/9121041 by East Anglia University user on 24 November 2026

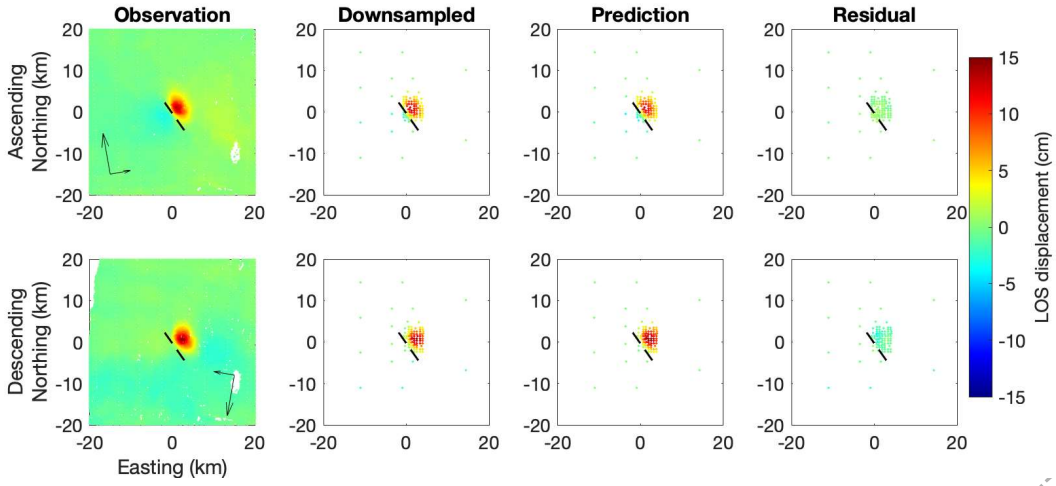

497

498 Figure 4. Coseismic displacement observations, downsampled data, model predictions, and

499 residuals for the ascending track (upper panel) and descending track (lower panel). The black

500 dashed line shows the fault trace determined from uniform-slip modelling in this study.

501

ORIGINAL UNEDITED MANUSCRIPT

Downloaded from academic.oup.com/gji/advance-article/doi/10.1093/gji/ggag516/9121041 by East Anglia University user on 24 November 2026

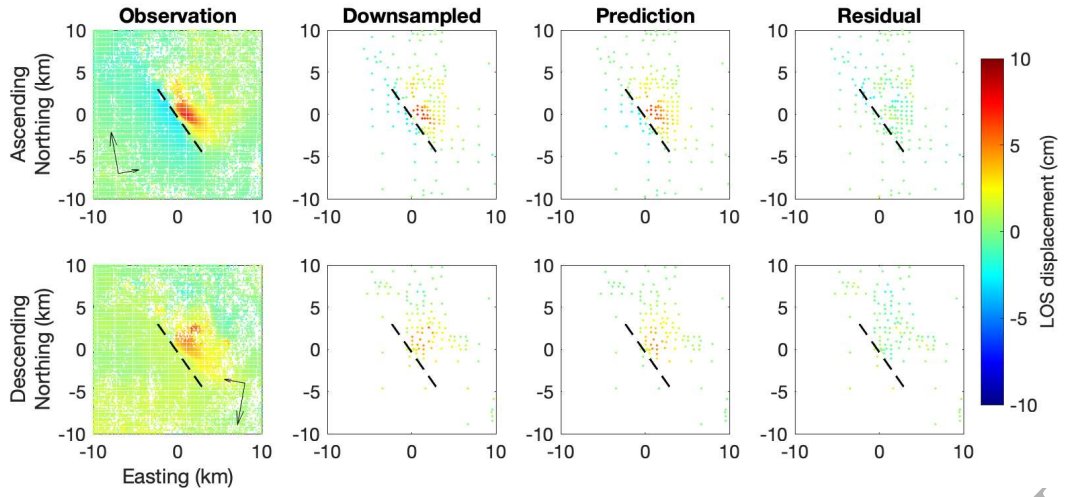

502

503 Figure 5. Same as Figure 4, but for the cumulative ~5 years of postseismic displacement.

504

ORIGINAL UNEDITED MANUSCRIPT

Downloaded from academic.oup.com/gji/advance-article/doi/10.1093/gji/ggag516/9121041 by East Anglia University user on 24 November 2026

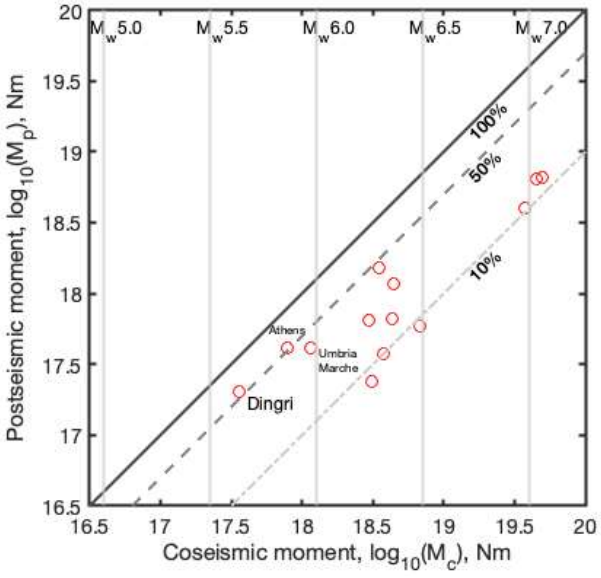

505

506 Figure 6. Compilation of postseismic-to-coseismic moment ratio (PCMR) determined by
507 geodetic studies of normal-faulting earthquakes (Table S2). The 2020 Mw 5.6 Dingri
508 earthquake stands out as having the highest PCMR.

509

ORIGINAL UNEDITED MANUSCRIPT

Downloaded from academic.oup.com/gji/advance-article/doi/10.1093/gji/ggag516/9121041 by East Anglia University user on 24 November 2026

510 Table 1. Fault geometry and source parameters derived from Bayesian inversion, assuming
511 uniform slip on a fault plane buried in an elastic half-space. GCMT and USGS solutions for the
512 2020 Mw 5.6 earthquake are also included for comparison. The reference point is (87.387°,
513 28.666°).

model	X (km)	Y (km)	Strike (°)	Dip (°)	Rake (°)	Slip (m)	Length (km)	Top (km)	Bottom (km)	Moment (10^{17} Nm)	Mw
This study	0.023 ± 0.04	−0.357 ± 0.05	324.82±0.81	57.77 ± 0.97	−89.33 ± 2.59	0.81 ± 0.04	2.863 ± 0.08	1.917 ± 0.04	5.683 ± 0.16	3.621	5.64
USGS	-7.736	-8.448	343/180	49/42	-101/-77	–	–	–	–	4.358	5.69
GCMT	3.222	-17.316	345/184	45/47	-103/-77	–	–	–	–	3.884	5.66

514

ORIGINAL UNEDITED MANUSCRIPT

Downloaded from academic.oup.com/gji/advance-article/doi/10.1093/gji/ggag516/9121041 by East Anglia University user on 24 November 2026